Nanoscale Advances

PAPER

View Article Online
View Journal | View Issue

Cite this: *Nanoscale Adv.*, 2025, 7, 5313

Electrochemical investigation of $Ti_3C_2T_x$ (MXene), N-$Ti_3C_2T_x$, and the $Ti_3C_2T_x/Co_3O_4$ hybrid composite deposited on carbon cloth for use as anode materials in flexible supercapacitors†

Lan Nguyen,[a] Adnan Ali, *[a] Brahim Aissa, [c] Sosiawati Teke,[ab] Roshan Mangal Bhattarai, [a] Avik Denra,[a] Oai Quoc Vu [a] and Young Sun Mok *[a]

Received 9th December 2024
Accepted 19th May 2025

DOI: 10.1039/d4na01024h

rsc.li/nanoscale-advances

Supercapacitors have been studied as a potential complementary technology for rechargeable batteries, fuel cells, and dielectric capacitors. Wearable energy storage systems need freestanding, flexible electrodes for maximum functioning. Optimal energy storage system performance demands an optimal balance between mechanical component flexibility and electrode energy storage and release efficiency. This work specifically focuses on investigation and comparison of the electrochemical performance of the synthesized $Ti_3C_2T_x$, N-$Ti_3C_2T_x$, and the $Ti_3C_2T_x/Co_3O_4$ hybrid composite. Co_3O_4 NPs have been synthesized using an innovative and cost-effective novel synthesis route employing a "microplasma discharge reactor". This offers significant benefits, including the effective prevention of hazardous reducing agent generation in comparison to other routes. Upon exposure to 1 A g^{-1} current density, the $Ti_3C_2T_x/Co_3O_4$ hybrid composite electrode demonstrates a maximum gravimetric capacity of 128 F g^{-1} and a specific capacitance of 576.7 F g^{-1}, exhibiting a significant 95.06% increase in specific capacitance compared to $Ti_3C_2T_x$. Furthermore, from the kinetic analysis of the CV curves, it has been noticed that the contributions of the diffusion-controlled and pseudocapacitive-controlled processes are 60% and 40%, respectively, in the charge storage for the applied $Ti_3C_2T_x/Co_3O_4$ hybrid composite electrode.

1. Introduction

In today's world, the growing concern over global warming has sparked interest among researchers worldwide in the development of eco-friendly materials and innovative devices. A diverse array of energy storage devices are available to cater to different requirements, including supercapacitors, batteries, fuel cells, solar cells, wind energy devices, and hydropower devices. These technologies provide various solutions for energy storage needs.[1–3] Out of these technologies, wind energy and solar energy rely on weather and sunlight, presenting certain limitations.[4,5] In some cases, when it comes to power requirements, supercapacitors are the most practical option[6] because supercapacitors have an edge in energy, power density, lifespan, safety, and durability.[7] Supercapacitors possess impressive qualities such as high specific capacitance values, quick charge–discharge characteristics, and promising storage capacity for numerous applications.[8] Supercapacitors are categorized into two types: electric double-layer capacitors (EDLCs) and pseudocapacitors. In EDLCs, carbon resources such as graphene or carbon nanotubes are commonly utilized as electrode materials.[9] On the other hand, pseudocapacitors rely on redox reaction processes.[10] Pseudocapacitors have garnered significant interest for their impressive specific capacitance and rapid redox kinetics.[11] The exchange of ions between the electrode material and the electrolyte leads to the storage of charge in the electrode. This deposition of ions on the electrode surface affects electrochemical performance due to their physical and chemical characteristics.[12,13] Thus, the selection of the electrode material plays a critical role in determining the electrochemical properties of a supercapacitor, leading scientists to explore a wide variety of materials in order to get optimal capacitance results.[14,15] Recent investigations by researchers have focused on materials, such as metal oxides, metal–organic frameworks (MOFs), and two-dimensional (2D) materials such as graphene, MXenes, and their composites.[16] Notably, MXenes, which include carbonitrides, nitrides, and 2D transition metal carbides (TMCs), have garnered significant attention due to their remarkable electrical conductivity, mechanical properties, and surface functionalities.[17–20] Supercapacitors have shown promising results with $Ti_3C_2T_x$ (MXene) applied as an electrode.

---

[a] *Department of Chemical Engineering, Jeju National University, Jeju 63243, Republic of Korea. E-mail: adali@jejunu.ac.kr; smokie@jejunu.ac.kr*

[b] *Department of Physics, Halu Oleo University, Kendari-93132, Republic of Indonesia*

[c] *Qatar Environment and Energy Research Institute (QEERI), Hamad Bin Khalifa University (HBKU), Qatar Foundation, Doha 5825, Qatar*

† Electronic supplementary information (ESI) available. See DOI: **https://doi.org/10.1039/d4na01024h**

The flexible surface chemistry and high conductivity of $Ti_3C_2T_x$ enable the efficient transport of electrolyte ions.[15,21–23] The presence of multiple functional groups in $Ti_3C_2T_x$ allows it to demonstrate hydrophilic behavior.[24–28]

Studies have explored the integration of transition metal oxides and sulfides with MXene-based supercapacitors to enhance their energy storage capabilities.[29–34] Among the metal oxides, the face-centered cubic compound Co_3O_4 has gained a lot of attention for its possible use as an electrode material in energy storage devices.[11,35–38] It has been demonstrated that, in comparison to bulk materials, nanoscale materials with small particle size and a high surface/volume ratio can increase the number of active sites, decreasing the mass and charge diffusion distances, which improve electrochemical performances.[39,40] The electrochemical properties of Co_3O_4 have garnered significant interest from researchers. Its mixed-valence state and spinel structure facilitate ion diffusion, leading to improved stability and electrochemical performance over CoO in supercapacitor applications. The redox reactions of the Co^{3+}/Co^{2+} pair are pivotal to pseudocapacitance, which is responsible for the high specific capacitance of Co_3O_4.[41–43] Co_3O_4 nanoparticle synthesis *via* hydrothermal,[44] sol–gel,[45] solvothermal,[46] spray pyrolysis,[47] microemulsion,[48] biological templating,[29] and electrodeposition methods has been reported.[29] In this research, Co_3O_4 nanoparticles (NPs) have been synthesized using a novel device called the microplasma discharge reactor (MPR). MPR is a direct, cost-effective, and reliable device that functions at standard atmospheric pressure and produces nanoparticles with outstanding uniformity.[49] The interlayer spacing in $Ti_3C_2T_x$ nanosheets and the presence of surface terminations, such as functional groups, along with the large surface area of Co_3O_4 nanoparticles, contribute to their superior ability to enhance charge transfer and redox reaction kinetics. Consequently, the potential for numerous redox reaction sites leads to enhanced electrochemical performance. In this work, we have adopted the hybridization approach using Co_3O_4 nanoparticles coupled with $Ti_3T_2C_x$ to enhance the stability of MXene-based electrodes while concurrently maintaining their exceptional electrochemical properties. Herein, $Ti_3C_2T_x$, N-$Ti_3C_2T_x$ and the $Ti_3C_2T_x/Co_3O_4$ hybrid composite have been successfully synthesized. Co_3O_4 synthesized using the MPR was incorporated in between and on the outer surfaces of the 2D-$Ti_3C_2T_x$ nanosheets for energy storage application in supercapacitors. The structure, morphology, and composition of the synthesized materials were thoroughly investigated using scanning electron microscopy (SEM), energy dispersive spectroscopy (EDS), X-ray diffraction (XRD) analysis, Raman spectroscopy, transmission electron microscopy (TEM) and X-ray photoelectron spectroscopy (XPS), while their electrochemical performance was tested on an AutoLab PGSTAT204N, Metrohm electrochemical workstation in a three-electrode configuration system by measuring the Cyclic Voltammetry (CV), Galvanic Charging/Discharging (GCD), and Electrochemical Impedance Spectroscopy (EIS) profiles. For investigating the role of functional groups, FTIR spectra of $Ti_3C_2T_x$, Co_3O_4 and the hybrid nanocomposite $Ti_3C_2T_x/Co_3O_4$ were obtained. It has been observed through thorough investigation that the $Ti_3C_2T_x/Co_3O_4$ hybrid composite performance as an anode is the best compared to $Ti_3C_2T_x$ and N-$Ti_3C_2T_x$.

2. Experimental

2.1. Materials and preparation of the multilayer $Ti_3C_2T_x$ MXene

MAX phase titanium aluminum carbide (Ti_3AlC_2) was synthesized by mixing Ti_2AlC (Sigma Aldrich) and TiC in a 1 : 1 mole ratio. The mixture was ball-milled for 24 hours. After ball milling, the mixture was sintered for 2 hours at 1300 °C in argon at 50 sccm. The tiny Ti_3AlC_2 pellet was cooled to room temperature. The material was carefully milled and sifted. Ti_3AlC_2 powder with a particle size of ≤40 μm was made using this process. Selective etching of Ti_3AlC_2 using HF (Fisher Scientific). Over 5 minutes, 2 g of sieved Ti_3AlC_2 was added to a 20 milliliter solution of 48–51% HF. The mixture was stirred at 250 rpm with a magnetic stirrer on a hot plate at 40 °C for 72 hours. The reaction mixture was washed with deionized water (DIW) by centrifugation at 3500 rpm for 5 minutes each time. After each spinning, the acidic supernatant was separated and additional DIW was added and centrifuged. At pH 5, the process stopped. The whole procedure produced multilayer MXene (m-$Ti_3C_2T_x$) flakes. The solution was vacuum-filtered to extract m-$Ti_3C_2T_x$ using a Celgard®3501 polypropylene membrane with a thickness of 25 μm and pore size of 0.064 μm. The powder was furnace-dried at 80 °C under normal conditions.

2.2. Preparation of exfoliated $Ti_3C_2T_x$ MXene (d-$Ti_3C_2T_x$) from m-$Ti_3C_2T_x$

A 300 mg sample of finely ground multilayer $Ti_3C_2T_x$ powder was added with 50 mL of degassed deionized water. The mixture was then sonicated for one hour using a Cole Parmer 750 watt ultrasonic homogenizer, set at 65% amplitude with an on–off cycle of 5 seconds on and 2 seconds off. During sonication, a steady argon flow of 10 sccm was maintained, and the container was kept in an ice bath to prevent temperature rise and potential oxidation of $Ti_3C_2T_x$. Following sonication, the solution underwent centrifugation at 3500 rpm for 30 minutes to separate the d-$Ti_3C_2T_x$ flakes. The resulting supernatant was then frozen at −50 °C for 20 minutes and subsequently freeze-dried overnight using a freeze dryer system (FDTE-8012).

2.3. Preparation of nitrogen doped $Ti_3C_2T_x$, MXene (N-$Ti_3C_2T_x$)

To synthesize N-$Ti_3C_2T_x$, a solution was prepared by adding 100 mg of $Ti_3C_2T_x$ in 50 mL of deionized water. Subsequently, a 5 mg quantity of urea was introduced into the mixture while maintaining constant stirring. The mixture was transferred to a hydrothermal Teflon-lined autoclave unit and underwent a reaction with urea at a temperature of 180 °C for a duration of 18 hours. Subsequently, the autoclave underwent a cooling process until it reached the ambient temperature, resulting in nitrogen doped $Ti_3C_2T_x$. The N-$Ti_3C_2T_x$ was subjected to several DIW washes and then centrifuged at a speed of 5000 rpm for

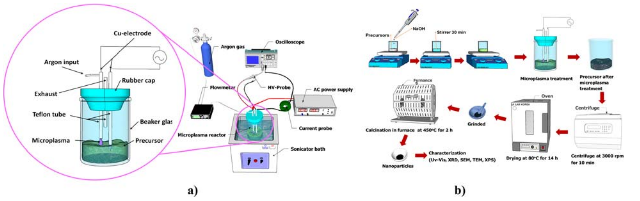

Fig. 1 (a) Schematic diagram of the MPR setup and (b) synthesis process of cobalt oxide nanoparticles.

a duration of 5 minutes. The N-$Ti_3C_2T_x$ sediment was subjected to freezing at a temperature of −55 °C for a duration of 24 hours. Subsequently, it was subjected to lyophilization using an FDTE-8012 freeze dryer to remove the ice.

2.4. Preparation of cobalt oxide nanoparticles (Co_3O_4 NPs)

Cobalt oxide nanoparticles were prepared by an economic technique, microplasma reactor discharge.[49] A 0.01 M solution of ($Co(NO_3)_2\cdot 6H_2O$) was added to 25 mL of DIW. Then, 1 M NaOH was introduced into the pH = 10 solution. A magnetic stirrer was used to agitate the mixture for 30 minutes at 100 rpm in an ambient environment. The sample was placed in an ultrasonication bath set at a frequency of 28 kHz and treated with plasma for 25 minutes. After centrifuging, the resultant solution was cleaned with ethanol and allowed to dry for 14 hours at 80 °C in an oven. Ultimately, the powder was ground and then air-fired for two hours at 450 °C (3.5 °C per minute) in a furnace. The step-by-step process of generating Co_3O_4 NPs is schematically shown in Fig. 1. Detailed explanation of the MPR mechanism of producing nanoparticles is given in the ESI,† and the mechanism is schematically shown in Fig. S1(a).† The size controlled Co_3O_4 nanoparticle synthesis *via* the MPR synthesis technique and particle size distribution analysis are given in Fig. S1(b).† Additionally, in the ESI,† the cost estimation calculation per gram Co_3O_4 nanoparticles *via* the MPR technique is provided, which is $7 per gram.

In this step, the $Ti_3C_2T_x/Co_3O_4$ hybrid composite was synthesized by adding 20 mg of $Ti_3C_2T_x$ and 5 mg of Co_3O_4 in 30 mL of DIW. The mixture underwent sonication in a bath for 30 minutes at room temperature. Following bath sonication, the mixture was placed in a Teflon hydrothermal unit. The hydrothermal unit was placed in a furnace and heated to 180 °C for a duration of 18 hours. It was then allowed to cool down to ambient room temperature. The resulting dispersion was centrifuged at a speed of 5000 rpm for a duration of 3 minutes, and this procedure was repeated a total of 4 times. The sediment was subsequently dried at 80 °C for 8 hours. After that, the dried powder of $Ti_3C_2T_x/Co_3O_4$ was ground in a mortar and then subjected to calcination in an argon environment at 400 °C for 2 hours.

3. Preparation of electrodes

Before applying the active material mixture as the electrode on carbon cloth (CC), it went through a 10 hour drying process at 80 °C, and after it was treated with HNO_3, rinsed with DIW, ethanol, and acetone, and then desiccated. The anode electrode material was prepared by combining $Ti_3C_2T_x$, N-$Ti_3C_2T_x$ and the $Ti_3C_2T_x/Co_3O_4$ hybrid composite one by one with Super P and polyvinylidene fluoride (PVDF) in a proportion of 8 : 1 : 1.5 drops of *N*-methyl-2-pyrrolidone (NMP) was added to the mixture to prepare the slurry. It was then ground for 30 minutes in a mortar. After evenly applying the electrode material onto a 2.25 cm^2 section of the CC substrate, it underwent a thorough drying process for 8 hours at 100 °C in a vacuum furnace. The loaded active mass was approximately 5.6 mg. Fig. 2 presents a detailed schematic diagram showcasing the various steps in the synthesis of the $Ti_3C_2T_x/Co_3O_4$ hybrid composite. This includes the preparation of the slurry and the subsequent deposition process.

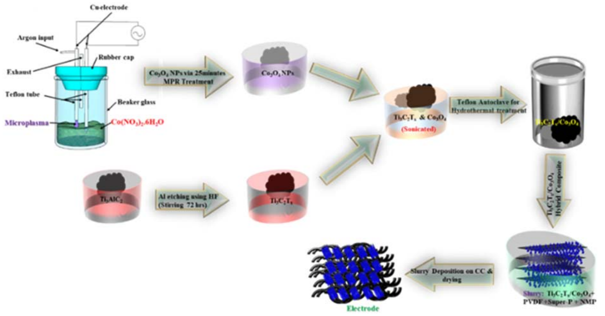

Fig. 2 Schematic diagram of $Ti_3C_2T_x/Co_3O_4$ hybrid composite deposition on carbon cloth.

4. Materials characterization

The morphology analysis was conducted using field emission scanning electron microscopy (FE-SEM) with a TESCAN MIRA3. The chemical compositions were evaluated through elemental mapping (TESCAN, MIRA3) and energy-dispersive spectroscopy (EDS) at 15 kV. The XRD technique was utilized to investigate the structure of synthesized $Ti_3C_2T_x$ (unexfoliated & exfoliated), Co_3O_4 NPs, and the Ti_3AlC_2/Co_3O_4 hybrid composite. A PANanalytical Empyrean XRD instrument was employed, using Cu Kα1 radiation at λ = 0.15406 nm. The scan range for this investigation was 2θ values of 5° to 60°. To accurately determine the elemental composition, chemical state, and electronic structure of the materials, a Thermo Fisher Scientific Theta Probe K-ALPHA + XPS system using monochromatic Al Kα radiation with a wavelength of 1486.6 eV at 12 kV at the KBSI Busan Center was utilized. Additionally, Raman spectroscopy and FTIR characterization experiments were carried out to gain a better understanding of the role of structure and functional groups in energy storage. For the electrochemical analysis, a three-electrode system was employed, which comprised an Ag/AgCl reference electrode, a platinum wire counter electrode, and a working electrode prepared according to the method outlined in the Preparation of electrodes section, all immersed in 1 M H_2SO_4. The performance of the electrode materials was assessed using an AutoLab PGSTAT204N Metrohm electrochemical workstation, employing techniques such as cyclic voltammetry (CV), galvanostatic charge–discharge (GCD), and electrochemical impedance spectroscopy (EIS).

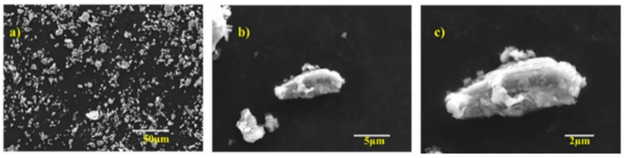

Fig. 3 Low to high resolution FESEM images of Ti_3AlC_2 (a)–(c).

5. Results and discussion

5.1. Microstructure and phase analysis

The morphology of Ti_3AlC_2 was analyzed using FE-SEM. As depicted in Fig. 3 (a–c) and S2,† the Ti_3AlC_2 particles are significantly smaller than 40 μm, which is beneficial for selectively etching away Al from the MAX phase within an optimized minimal duration.

The etched Ti_3AlC_2 is depicted in Fig. 4(a–c) and S3† through a series of FESEM images that vary from low to high resolution. After the etching process, the weakly bonded Al is almost etched away, resulting in unexfoliated, stacked flakes of $Ti_3C_2T_x$. The process of selectively etching Al from Ti_3AlC_2 to produce $Ti_3C_2T_x$ presents a series of intricate challenges. The etchant employed here was 48% HF. Residual Al atoms still exist within the $Ti_3C_2T_x$ framework, potentially as a result of incomplete chemical reactions or intrinsic physical barriers associated with the layered architecture. The surface termination groups, including –OH, –F, or –O, incorporated during the etching process may interact with residual Al, thereby complicating its thorough elimination. Probe sonication was conducted under an argon flow to prevent oxidation and to enhance the interlayer spacing among the flakes. In Fig. S4,† lattice spacing increase of $Ti_3C_2T_x$ is schematically shown after Ti_3AlC_2 etching. High-resolution transmission electron microscopy (HRTEM) images of $Ti_3C_2T_x$ are shown in Fig. S5,† which show the few layers and multilayers of $Ti_3C_2T_x$. HRTEM images of Co_3O_4 nanoparticles synthesized using the microplasma discharge reactor are given in Fig. 4(d)–(e). Distinct lattice planes at approximately 0.45, 0.36, and 0.19 nm have been discerned upon examination. The crystalline structure within the Co_3O_4 nanoparticle is confirmed by the fast Fourier transform (FFT) image shown in Fig. 4(e) inset. The Co_3O_4 nanoparticle (NP) sample size is definitively smaller than 15 nm. Fig. 4(f) presents the color mapping images of the nanobulk, corresponding to the high-angle annular dark-field energy-dispersive spectroscopy (HAADF-EDS) results, highlighting the presence of oxygen and cobalt in the Co_3O_4 NP sample. EDS analysis results of $Ti_3C_2T_x$ are given in Fig. S6.† Fig. 4(g)–(i) display images of the $Ti_3C_2T_x/Co_3O_4$ hybrid composite at varying resolutions, from low to high. The FESEM analysis indicates that the Co_3O_4 nanoparticles have been successfully intercalated among the $Ti_3C_2T_x$ flakes due to their size being smaller than 15 nm. The integration is designed to prevent the restacking of $Ti_3C_2T_x$ flakes, thereby preserving their conductivity and high specific surface area. This contributes significantly to the properties of the hybrid composite, which is advantageous for redox reactions in electrochemical analysis. Fig. 4(j) shows the EDS spectrum of the hybrid composite $Ti_3C_2T_x/Co_3O_4$, which confirms the presence of Ti, Co, C, O, Cl, and Al peaks among others, which is an indication that it is not 100% etched away. The EDS mapping of the hybrid composite $Ti_3C_2T_x/Co_3O_4$ is given in Fig. S7.† It is obvious that in the hybrid composite there are two significant peaks at around 4.5 keV and 4.9 keV corresponding to Ti. Its prominent sharp peaks with high intensity indicate that the Ti concentration is high. Similarly, three distinct peaks corresponding to Co in the EDS spectrum of the hybrid composite appeared at 6.9 keV and 7.4 keV, and a lesser intensity peak appeared around 0.8 keV. The intensity of the Co peaks suggests that it is present in significant quantities, but the titanium content is more. There is a noticeable peak at around 0.5 keV in the EDS spectrum of O. This is because, in the hybrid composite, Co is present as oxide, and a small amount of $Ti_3C_2T_x$ is converted to TiO_2 as well. Oxygen is present,[50] however, at a lower concentration, as evidenced by the peak height that is smaller than that of Ti and Co. Cl and Al impurities supplement the main components of the hybrid composite, which also include Ti, Co, C, and O. Also, these results are supported by the XPS and XRD analysis results of the hybrid composite.

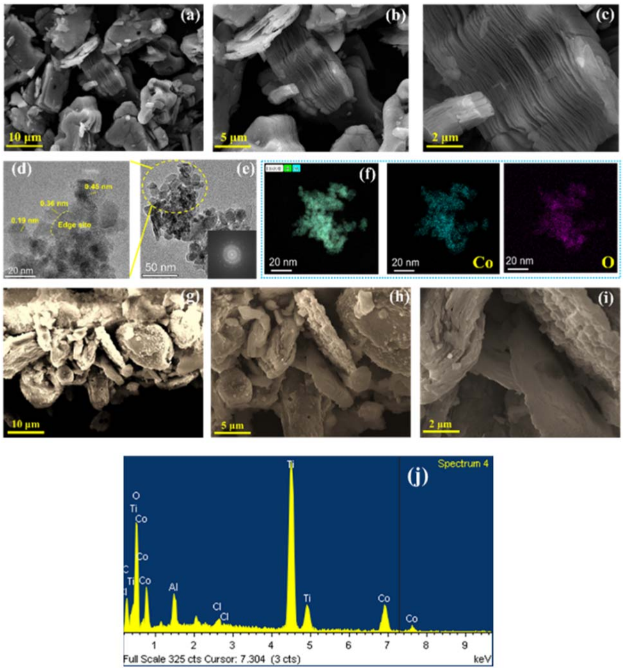

Fig. 4 (a)–(c) FE-SEM images of $Ti_3C_2T_x$, (d) HRTEM micrograph of Co_3O_4 NPs, (e) TEM image of Co_3O_4 NPs with the corresponding FFT shown in the inset, (f) HAADF-EDS color mapping of Co NPs showing Co and O elements, (g)–(i) FE-SEM images of the $Ti_3C_2T_x/Co_3O_4$ hybrid composite, (j) EDS analysis of the $Ti_3C_2T_x/Co_3O_4$ hybrid composite.

5.2. Structural analysis *via* X-ray diffraction

The XRD patterns for $Ti_3C_2T_x$, both unexfoliated and exfoliated, are presented in Fig. 5. The diffraction peak positions of MAX correspond well with the simulation based on standard data (JCPDS no. 00-052-0875). Observations indicate that in unexfoliated $Ti_3C_2T_x$ the corresponding peaks are narrower. However,

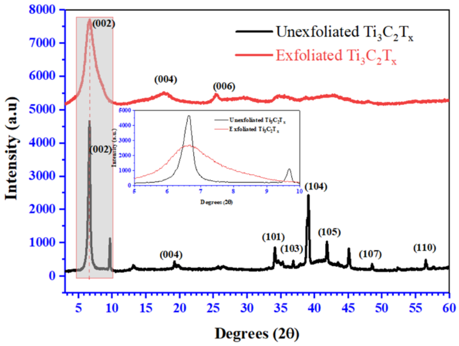

Fig. 5 Unexfoliated and exfoliated $Ti_3C_2T_x$ XRD patterns.

after the exfoliation of $Ti_3C_2T_x$, these signature peaks broaden, and their intensities decrease. Following chemical exfoliation with HF, the (002) peak of $Ti_3C_2T_x$ broadens and shifts to a lower angle of 6.2° from its original position of 9.4°, and the diffraction peak disappears, confirming the transformation of the MAX (Ti_3AlC_2) phase into the MXene ($Ti_3C_2T_x$) phase. Similarly, the diffraction peak positions of Co_3O_4 nanoparticles corresponded well with the simulation based on standard data (JCPDS no. 00-043-1003). Further on, XRD analysis of the $Ti_3C_2T_x/Co_3O_4$ hybrid composite shows the (002) diffraction peak which is shifted further to $2\theta = 5.7°$, signifying an increase in interlayer spacing. This is due to the insertion of Co_3O_4 nanoparticles between the $Ti_3C_2T_x$ layers. For more deep structural investigation and insight, Raman spectroscopy was carried out to support the findings of the XRD analysis. Raman spectroscopy analysis provides detailed information about the chemical structure of $Ti_3C_2T_x$, CO_3O_4 and the hybrid composite $Ti_3C_2T_x/Co_3O_4$, and the spectra are presented in Fig. S9.†

5.3. Structural and compositional analyses *via* XRD and XPS

XRD analysis was conducted for hydrothermally synthesized N-$Ti_3C_2T_x$ and $Ti_3C_2T_x/Co_3O_4$ hybrid composites from exfoliated $Ti_3C_2T_x$ and MRP synthesized Co_3O_4 nanoparticles to examine and contrast the structural alterations, as shown in Fig. 6(a).[15] The XRD pattern of the hybrid composite indicates the characteristic peaks of both $Ti_3C_2T_x$ and Co_3O_4 phases. A subtle shift toward lower angles was observed in the peaks, and some peaks overlapped and broadened in the XRD pattern of the $Ti_3C_2T_x/Co_3O_4$ composite. This indicates that the Co_3O_4 nanoparticles were effectively incorporated into the $Ti_3C_2T_x$ nanosheets.[11,49] The XRD pattern of N-$Ti_3C_2T_x$ is given in Fig. S8(a).†

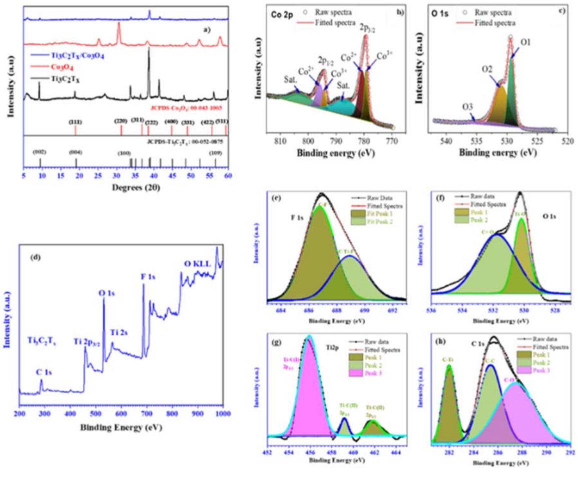

Fig. 6 (a) XRD patterns of $Ti_3C_2T_x$, Co_3O_4 NPs, and the $Ti_3C_2T_x/Co_3O_4$ hybrid composite, (b) and (c) XPS spectra of Co_3O_4 core levels, (d), (e)–(h) XPS survey and core level spectra of F 1s, O 1s, Ti 2p and C 1s respectively.

XPS analysis was conducted on the synthesized samples to examine their chemical states and composition. In Co_3O_4, the binding energy (BE) peaks of Co $2p_{3/2}$ and Co $2p_{1/2}$ can be observed in the range of 779.38 to 779.68 and 794.38 to 794.68 eV, respectively, as shown in Fig. 6(b). The 2p binding energies for CoO and Co_3O_4 spinel phases are the same, which poses a challenge in distinguishing between the two. Energy separation (ΔE) between the Co $2p_{3/2}$ and Co $2p_{1/2}$ peaks amounts to 15.0 eV for Co_3O_4 and 16.0 eV for CoO. This 1.0 eV difference is significant as it distinguishes CoO from Co_3O_4. Apart from that, the two shake-up satellites distinguish the Co_3O_4 spinel phase.[51,52] Fig. 6(c) shows the XPS analysis of O 1s. In the context of nanoparticle materials used in catalysis, energy conversion/storage, and sensors, acknowledging the presence of oxygen vacancies is crucial.[53,54] The O 1s spectrum reveals a peak for O1, which signifies the presence of metal oxides (Co–O), within a binding energy range from 529.18 to 529.48 eV. An additional peak for O2 suggests the existence of oxygen vacancies, with a binding energy between 530.68 and 530.88 eV. The O3 peak is a prominent feature indicating the presence of surface hydroxyl molecules (Co–OH) with a binding energy between 533.48 and 534.68 eV. The presence of the O1 peak in the XPS profiles confirms the successful synthesis of Co_3O_4 using the microplasma discharge reactor.[49,55,56] Fig. 6(d) presents the XPS survey spectra of the etched and exfoliated $Ti_3C_2T_x$. The analysis of the XPS spectra for $Ti_3C_2T_x$ required the application of curve fitting to derive pertinent information. The bonding peaks within the F 1s, O 1s, Ti 2p, and C 1s XPS spectra have been precisely identified through meticulous analysis.[57,58]

The exfoliated layers of Ti_3C_2 are coated with terminal species and adsorbates on their surfaces. Distinguishing termination species from adsorbates is essential, as they significantly impact the synthesis of exfoliated Ti_3C_2 layers. Terminal species function analogously to the Al layer in Ti_3AlC_2, serving comparable roles in the material's structure and properties. Understanding the role of terminal species is crucial for creating appropriate conditions for electron redistribution in Ti_3C_2 layers and enhancing the strength of Ti–C covalent bonds.[57] Fig. 6(e) displays the F 1s spectrum obtained from the termination species present on the surface of $Ti_3C_2T_x$. Considering the variance in slope between the low and high binding energy sides, it becomes evident that the fitting curve must accommodate two distinct peaks. Two distinct peaks were detected; one at 686.7 eV, signifying the presence of C–F bonds, and another at 688.94 eV, indicative of C-Ti–F bonds.[59,60] Fig. 6(f) illustrates the O 1s spectrum, which is characterized by two distinct peaks. A meticulous examination of the ascending trend on the lower binding energy side reveals a solitary bonding peak at 530.1 eV, suggestive of a Ti–O bond. The peak at 531.79 eV overlaps with the one at 530.1 eV, associated with C=O, obscuring the observation of the rising gradient on the lower binding energy side of the peak.[59,61] Fig. 6(g) displays the Ti 2p spectrum. Curve fitting of this spectrum can be quite complex due to the presence of two XPS peaks, $2p_{3/2}$ and $2p_{1/2}$, which exhibit different intensities. The peak at 455.9 eV is less intense than the peak at 461.63 eV. A notable difference of approximately 6.0 eV in binding energy between these two peaks simplifies the curve fitting process. Additionally, there is a peak at the higher binding energy side of Ti $2p_{3/2}$, which does not exhibit any additional features.[57,58] Fig. 6(h) displays the C 1s XPS spectrum. The peak observed at 282.0 eV within the C 1s spectrum suggests the presence of carbide materials, particularly Ti–C. Additionally, peaks at binding energies of 285.66 eV and 287.65 eV are present, corresponding to C–C and C–O bonds, respectively. The latter peaks, found at higher binding energies, are typically linked to graphite.[62] Due to the multistage synthesis process of exfoliated $Ti_3C_2T_x$, there is a high likelihood of contamination and the presence of residual unetched Ti_3AlC_2. From the C 1s spectrum, it is evident that the peak associated with carbide materials is distinct from any contaminations or impurities. There is a noticeable difference in the steepness of the rising slope on the low BE side compared to the high BE peaks.[58] For N-$Ti_3C_2T_x$, XPS analysis results are given in Fig. S8(b),† and it has been observed that doped nitrogen has bonded with Ti as well as with C and O present in $Ti_3C_2T_x$.

6. Electrochemical characterization by CV, GCD, and EIS

The electrodes $Ti_3C_2T_x$, N-$Ti_3C_2T_x$ and $Ti_3C_2T_x/Co_3O_4$ deposited on CC were thoroughly analysed to investigate their electrochemical performance. For this, cyclic voltammetry (CV), galvanostatic charge–discharge (GCD), and electrochemical impedance spectroscopy (EIS) using a three-electrode system in a 1 M H_2SO_4 electrolyte have been performed.

At scan rates ranging from 10 to 50 mV s^{-1}, the CV curves for $Ti_3C_2T_x$, N-$Ti_3C_2T_x$, and $Ti_3C_2T_x/Co_3O_4$ electrodes have been obtained and are presented in Fig. 7(a)–(c). Based on the observations of the changes in redox peaks for the electrodes, the functional groups were more affected in a favorable manner by the $Ti_3C_2T_x/Co_3O_4$ electrode deposited on CC compared to $Ti_3C_2T_x$ and N-$Ti_3C_2T_x$ electrodes. CV curves of $Ti_3C_2T_x/Co_3O_4$ exhibit a handful of distinct redox peaks, which indicate the occurrence of pseudocapacitance. This pseudocapacitance was suitable with CV result when redox peak at −0.3 V stopping. In addition, the $Ti_3C_2T_x/Co_3O_4$ electrode demonstrates a longer discharge time compared to other electrodes, suggesting a higher specific capacitance. The CV profile of the electrode in Fig. 7(c) maintains a consistent shape even at higher scan rates. This indicates that the electrode exhibits exceptional rate performance, which may be attributed to its high stability and wettability. All CV curves exhibit distinct redox peaks, which are predominantly linked to the faradaic redox processes. The trend indicating higher anodic and cathodic peak intensities at increased scan rates suggests efficient charge transfer and minimal resistance at the electrode–electrolyte interface. At lower scan rates, redox reactions that rely on proton (H^+) insertion/desertion pathways from the electrolyte facilitate the diffusion of ions from the electrolyte into the accessible active sites in the electrode. Due to the interaction between hydronium ions (protons H^+) and –O, bonding and debonding occur. The processes of bonding and debonding are reversible, thereby enabling the reversibility of the Ti valence state. Therefore, the electrolyte is expected to demonstrate a pseudocapacitive effect during cyclic voltammetry measurements. With an increase in the scan rate, the anodic peak moves to a more positive potential, while the cathodic peak moves to a more negative potential. This shift is attributed to the insufficient time available for ions to intercalate into the electrode.[63] In comparison to bare CC and $Ti_3C_2T_x$/CC, the peak current has increased as the oxidation current density improved. The discharge behavior of individual electrodes was measured at current densities ranging from 1 to 5 A g^{-1}, as given in Fig. 7(d)–(f). The discharge time for the pristine $Ti_3C_2T_x$ electrode was approximately 35 seconds, whereas the N-$Ti_3C_2T_x$ electrode achieved a discharging time of up to 210 seconds. While for the hybrid composite electrode $Ti_3C_2T_x/Co_3O_4$, the discharging time extended to nearly 950 seconds. Similarly, for comparison, N-$Ti_3C_2T_x/Co_3O_4$ CV analysis has been carried out as well. Electrochemical analysis *i.e.* CV and GCD of the N-$Ti_3C_2T_x/Co_3O_4$ electrode applied on carbon cloth is given in Fig. S11.† A detailed discussion is given in the ESI† for N-$Ti_3C_2T_x/Co_3O_4$.

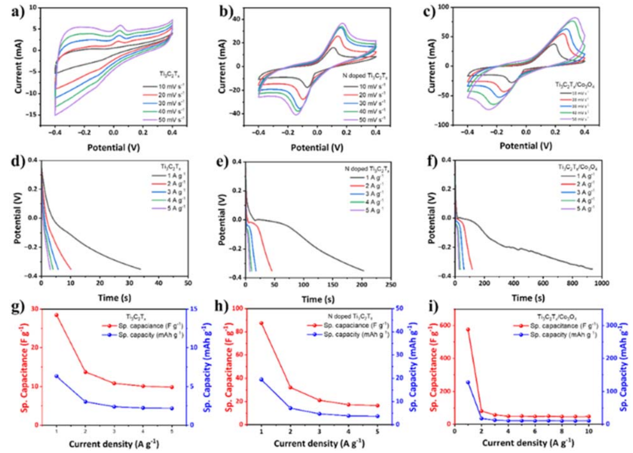

Fig. 7 (a)–(c) CV curves of different electrodes at 10 mV s^{-1} scan rate, (d)–(f) discharge curves of different electrodes from GCD analysis at 1 A g^{-1} current density, and (g)–(i) specific capacity and specific capacitance in terms of area and mass.

For the $Ti_3C_2T_x/Co_3O_4$ hybrid composite, applied as an anode material on carbon cloth using a 1 M H_2SO_4 electrolyte, the working mechanisms at positive and negative potentials involve both electrochemical double-layer formation and faradaic reactions, attributable to the pseudocapacitive properties of the electrode materials.

Fig. 7(f) shows the galvanostatic discharge of the $Ti_3C_2T_x/Co_3O_4$ hybrid composite sample at difference scan rates. To determine the specific capacitances and capacity of charge storage, the following equations were used:

$$C_g = \frac{2i\int V\mathrm{d}t}{m\Delta V} \tag{1}$$

$$C_F = \frac{2i\int V\mathrm{d}t}{m\Delta V^2} \tag{2}$$

where C_g is the gravimetric capacity (A h g^{-1}), C_F is the faradaic capacitance (F g^{-1}), i is the current applied (A), $\int V\mathrm{d}t$ is the integral area of the discharge curve (V s), m is the mass of the active material, and ΔV is the voltage difference in the discharge (V).

The specific capacitance values for each current density, obtained from the GCD curves, are shown in Fig. 7(g)–(i). At a current density of 1 A g^{-1}, the $Ti_3C_2T_x/Co_3O_4$ hybrid composite applied as an electrode has attained a maximum specific capacitance of 576.7 F g^{-1}. While pristine $Ti_3C_2T_x$ and N-$Ti_3C_2T_x$ have attained the maximum specific capacitance of 28.5 F g^{-1} and 87.5 F g^{-1} at a current density of 1 A g^{-1}, respectively.

7. Storage mechanism in the $Ti_3C_2T_x/Co_3O_4$ hybrid composite

Regarding ion adsorption/desorption, the reaction mechanism is usually complex, owing to the different metal oxide redox species. Nonetheless, the most probable charge storage processes during anodic and cathodic sweeps have been summarized here. $Ti_3C_2T_x$ being a 2D material with a layered structure, most of the charge storage is of electrochemical double-layer capacitance (EDLC) nature, due to its high surface area and enhanced conductivity. In the case of EDLC charge storage, the charges are stored electrostatically. $Ti_3C_2T_x$ also exhibits pseudocapacitive behavior due to the presence of functional groups (*e.g.*, –OH, –O, and –F) on its surface. Cations (H^+) from the H_2SO_4 electrolyte are attracted to the negatively charged $Ti_3C_2T_x$ surface during anodic sweep. While during cathodic sweep, the H^+ is de-intercalated or desorbed from the electrode material, and electrons are accepted from the external circuit. Likewise, oxidation and reduction of the surface attached functional groups occur during respective cycles, contributing to pseudocapacitance.[64,65]

In the case of the $Ti_3C_2T_x/Co_3O_4$ hybrid composite, the high surface area and conductivity of $Ti_3C_2T_x$ combine with the pseudocapacitive behavior of Co_3O_4. During anodic sweep, cations (H^+) are attracted to the electrode surface and oxidation of Co^{2+} to Co^{3+} or Co^{3+} to Co^{4+} occurs, contributing to pseudocapacitance. Likewise, during cathodic sweep, cations (H^+) are de-intercalated or desorbed from the electrode material. Reduction of Co^{3+} to Co^{2+} or Co^{4+} to Co^{3+} occurs, contributing to pseudocapacitance. For further exploring the effect of functional groups on the pseudocapacitance occurrence, FTIR analysis was carried out for pristine $Ti_3C_2T_x$, Co_3O_4 and the hybrid composite $Ti_3C_2T_x/Co_3O_4$. Detailed comparative explanation of the FTIR spectroscopy findings is given in Fig. S10.†

The $Ti_3C_2T_x$ layered exfoliated structure facilitates efficient ion transport to the Co_3O_4 sites, which is crucial for electrochemical reactions, resulting in rapid charge and discharge cycles. While effective electron transport to Co_3O_4 nanoparticles is ensured by $Ti_3C_2T_x$ superior electrical conductivity. This synergy of the hybrid composite enhances redox processes through reducing the internal resistance and improving the rate capability. In addition to this, the robust contact between $Ti_3C_2T_x$ and Co_3O_4 nanoparticles maintains the structural integrity of the hybrid composite during the volumetric changes of charging and discharging.[66]

During charging, electrons are transferred from the hybrid composite $Ti_3C_2T_x/Co_3O_4$ anode to the cathode. Concurrently, sulfate ions ($SO_4{}^{2-}$) from the H_2SO_4 electrolyte migrate towards the $Ti_3C_2T_x$ layers, forming an electrical double layer at the electrode/electrolyte interface.[67] The $SO_4{}^{2-}$ ions align near the positively charged surface of the $Ti_3C_2T_x/Co_3O_4$ anode. Similarly, during charging at the negative electrode, hydrogen ions (H^+) from the electrolyte are attracted towards its surface. An electric double layer forms at the electrode–electrolyte interface, with the H^+ ions aligning near the negatively charged electrode surface. Additionally, pseudocapacitive behavior involves the following faradaic redox reactions:[68–71]

$$Co^{2+} \rightleftharpoons Co^{3+} + e^- \tag{3}$$

$$Ti_3C_2O_x(OH)_yF_z + 1/2xe^- + 1/2xH^+ \rightleftharpoons Ti_3C_2O_{1/2x}(OH)_{y+1/2x}F_z \tag{4}$$

Additionally, in regard to the kinetic analysis aspects of charge storage mechanisms, it has involved the consideration of both the capacitive effects ($k_1\nu$) and the diffusion-controlled contributions ($k_2\nu^{0.5}$) in relation to the voltage and response current.[72] Respective percentile contributions from the $Ti_3C_2T_x/Co_3O_4$ hybrid composite applied as the anode material was calculated using Dunn's method, at different potential scan rates *i.e.* 10–50 mV s^{-1} and plotted, as shown in Fig. 8(a). Respective contributions were determined by analyzing the CV curves presented in Fig. 8(a), according to Dunn's method:[73,74]

$$i(\nu) = k_1\nu + k_2\nu^{0.5} \tag{5}$$

or

$$i(\nu)/\nu^{0.5} = k_1\nu^{0.5} + k_2 \tag{6}$$

where ν is the scan rate and i is the current. The slope of the fitting line is represented by k_1 and the intercept by k_2,

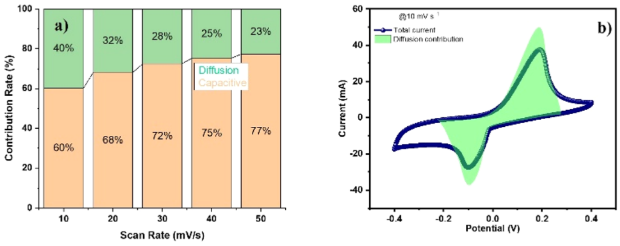

Fig. 8 (a) Contribution ratios of capacitances from the pseudocapacitive controlled reaction and diffusion-controlled reaction at scan rates of 10 to 50 mV s^{-1} and (b) the kinetic analysis of the pseudocapacitive and diffusion parts at a scan rate of 10 mV s^{-1}.

respectively, in the above equations. The quantitative study indicates that the CV curves at 10 mV s^{-1} have two sections capacity, as shown in Fig. 8(b). Fig. 8(b) shows a diffusion-controlled portion in the light green area and a capacitive-controlled region in the remaining area. As a result, at 10 mV s^{-1} and 50 mV s^{-1}, respectively, the diffusion-controlled portion of the total charge stored was 40% and 23%. It is shown that when the sweep rate increased from low to high, the diffusion-controlled proportions steadily dropped.

8. Charge transfer mechanism investigation by EIS measurement

For further elaboration and to make it easy for the researcher community to understand the charge transfer mechanism, CV and GCD curves at a current density of 1 A g^{-1} for CC and $Ti_3C_2T_x$, N-$Ti_3C_2T_x$ and the $Ti_3C_2T_x/Co_3O_4$ hybrid composite were recorded, and the plots are shown in Fig. 9(a) and (b). Similarly, the obtained maximum specific capacitance values were plotted and compared, as shown in Fig. 9(c). The charge transfer mechanism of $Ti_3C_2T_x$, N-$Ti_3C_2T_x$ and $Ti_3C_2T_x/Co_3O_4$ hybrid composite electrodes was investigated by conducting Electrochemical Impedance Spectroscopy (EIS) measurement. The obtained results for each electrode are shown in Fig. 9(d). EIS measurements provided further insights and understanding of the charge transfer mechanism. At higher frequencies, a smaller semicircle is observed for $Ti_3C_2T_x$, indicating faster charge transfer and lesser resistance. While at lower frequencies, a vertical line is observed, which is an indication of optimal capacitive behavior and effective ion diffusion within $Ti_3C_2T_x$. For N-$Ti_3C_2T_x$, the EIS measurement has shown a bit flattened and broadened semicircle at higher frequencies compared to pristine $Ti_3C_2T_x$, which is an indication that N-doping of $Ti_3C_2T_x$ has slightly enhanced the charge transfer resistance in the electrolyte. This behavior shown in the EIS plot indicates the charge transfer limitations at the interface of N-$Ti_3C_2T_x/H_2SO_4$ (electrode/electrolyte) for redox reactions. The flattened and broadened semicircle for N-$Ti_3C_2T_x$, relative to pristine $Ti_3C_2T_x$, indicates an increase in charge transfer resistance, potentially due to lattice distortions of $Ti_3C_2T_x$ due to nitrogen incorporation. At intermediate and low frequencies, the vertical line obtained is more pronounced compared to the pristine $Ti_3C_2T_x$. This behavior is an indication of enhanced capacitive behavior of N-$Ti_3C_2T_x$ due to diffusion-controlled processes and pseudocapacitance. This has possibly occurred due to the increased number of electroactive sites and surface wettability.

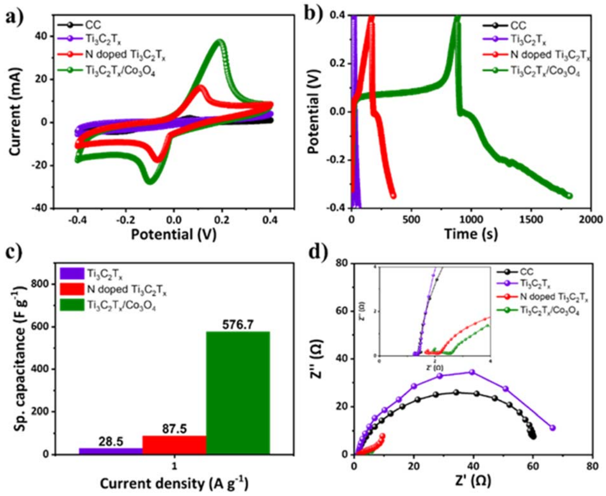

Fig. 9 CC, $Ti_3C_2T_x$, N-$Ti_3C_2T_x$ and $Ti_3C_2T_x/Co_3O_4$ electrodes: (a) CV curves at 10 mV s^{-1} scan rate, (b) discharge curves from GCD analysis at 1 A g^{-1} current density, (c) comparison of specific capacitance of $Ti_3C_2T_x$, N-$Ti_3C_2T_x$ and $Ti_3C_2T_x/Co_3O_4$ electrodes, and (d) EIS spectrum analysis of CC, $Ti_3C_2T_x$, N-$Ti_3C_2T_x$ and $Ti_3C_2T_x/Co_3O_4$.

The EIS spectra acquired for the $Ti_3C_2T_x/Co_3O_4$ hybrid composite exhibit the complementary and synergistic effects of the two materials. A somewhat more flattened and broadened semicircle than pristine $Ti_3C_2T_x$ and N-$Ti_3C_2T_x$ has been observed at higher frequencies. It has been observed that due to incorporation of Co_3O_4 NPs pseudocapacitance through redox reactions manifested Warburg impedance in the mid-frequency range and furthermore showed a transitioning into a sloping line at lower frequencies. This characteristic indicates an enhancement in energy storage capacity due to combined double-layer capacitance and pseudocapacitance.

9. Conclusions

Successful synthesis of $Ti_3C_2T_x$, N-doped $Ti_3C_2T_x$, and $Ti_3C_2T_x/Co_3O_4$ hybrid composite materials was achieved herein. Co_3O_4 nanoparticles were successfully synthesized using a novel device, microplasma discharge reactor, which is an eco-friendlier synthesis method. The synthesized materials were then employed as electrodes, using a slurry deposition technique involving the binder PVDF and Super P on carbon cloth. After careful analysis of $Ti_3C_2T_x$, N-$Ti_3C_2T_x$, and the $Ti_3C_2T_x/Co_3O_4$ hybrid composite (4 : 1), it was noted that the $Ti_3C_2T_x/Co_3O_4$ hybrid composite exhibited improved electrical conductivity. The incorporation of Co_3O_4 nanoparticles between the $Ti_3C_2T_x$ nanosheets, which prevented restacking, is the reason for enhancement in performance. The $Ti_3C_2T_x/Co_3O_4$ hybrid composite electrode showcased a remarkable specific capacitance of 576.7 F g^{-1} and a specific capacity of 128 A h g^{-1} when analyzed at a current density of 1 A g^{-1}. The specific capacitance was compared to the pristine $Ti_3C_2T_x$ electrode (28.5 F g^{-1}), and it showed a significant increase of 95.06% (20.23 times). The $Ti_3C_2T_x/Co_3O_4$ hybrid composite showed outstanding electrochemical performance, demonstrating its extensive potential for use in cutting-edge energy storage systems. To improve the electrochemical performance of $Ti_3C_2T_x$ and provide new perspectives for diverse applications, it is essential to achieve an ideal balance of Co_3O_4 nanoparticles.

Data availability

The data supporting this article have been included as part of the ESI.†

Author contributions

Lan Nguyen: synthesis of materials, electrochemical analysis, data curation, manuscript writing. Adnan Ali: conception, design, analysis, data curation, writing – original draft. Sosiawati Teke: synthesis of Co_3O_4 NPs *via* MPR, characterization. Roshan Mangal Bhattarai: assisted in electrochemical analysis, data curation. Avik Denra and Oai Vu Quoc: review and editing of the manuscript. Young Sun Mok: supervision, resources, funding acquisition, validation.

Conflicts of interest

The authors declare that they have no known competing financial interests or personal relationships that could have appeared to influence the work reported in this paper.

Acknowledgements

This work was supported by the National Research Foundation of Korea (NRF) grants funded by the Korea government (MSIT) (No. RS-2024-00405278 & No. 2022H1D3A2A02060361).

References

1 C. Azar, K. Lindgren and B. A. Andersson, *Energy Policy*, 2003, **31**, 961–976.

2 M. Z. Al Mahmud, Investigating Eco-Friendly Materials as Energy Storage Solutions, 2024, Available at SSRN: **https://ssrn.com/abstract=4743342**.

3 W. Zhao, S. J. B. Rubio, Y. Dang and S. L. Suib, *ACS ES&T Eng.*, 2022, **2**, 20–42.

4 A. Muzaffar, M. B. Ahamed and C. M. Hussain, *Renewable Sustainable Energy Rev.*, 2024, **195**, 114324.

5 B. Aïssa and A. Ali, *Sci. Rep.*, 2024, **14**, 4806.

6 S. Senthilkumar and R. K. Selvan, *Phys. Chem. Chem. Phys.*, 2014, **16**, 15692–15698.

7 M. Salanne, B. Rotenberg, K. Naoi, K. Kaneko, P.-L. Taberna, C. P. Grey, B. Dunn and P. Simon, *Nat. Energy*, 2016, **1**, 1–10.

8 R. Sonia, L. Phor, A. Kumar and S. Chahal, *J. Energy Storage*, 2024, **84**, 110698.

9 P. Simon, Y. Gogotsi and B. Dunn, *Science*, 2014, **343**, 1210–1211.

10 V. Augustyn, P. Simon and B. Dunn, *Energy Environ. Sci.*, 2014, **7**, 1597–1614.

11 S. Li, J. Fan, G. Xiao, S. Gao, K. Cui and Z. Chao, *Int. J. Hydrogen Energy*, 2022, **47**, 22663–22679.

12 L. Pan, D. Wang, J. Wang, Y. Chu, X. Li, W. Wang, N. Mitsuzaki, S. Jia and Z. Chen, *Phys. Chem. Chem. Phys.*, 2024, **26**, 9096–9111.

13 R. Tiwari, D. Kumar, D. K. Verma, K. Parwati, P. Ranjan, R. Rai, S. Krishnamoorthi and R. Khan, *J. Energy Storage*, 2024, **81**, 110361.

14 T. Ramachandran, S. S. Sana, K. D. Kumar, Y. A. Kumar, H. H. Hegazy and S. C. Kim, *J. Energy Storage*, 2023, **73**, 109096.

15 A. Ali, K. Hantanasirisakul, A. Abdala, P. Urbankowski, M.-Q. Zhao, B. Anasori, Y. Gogotsi, B. Aïssa and K. A. Mahmoud, *Langmuir*, 2018, **34**, 11325–11334.

16 A. Ali, K. Ali, K.-R. Kwon, M. T. Hyun and K. H. Choi, *J. Mater. Sci.: Mater. Electron.*, 2014, **25**, 1097–1104.

17 J. Yang, W. Bao, P. Jaumaux, S. Zhang, C. Wang and G. Wang, *Adv. Mater. Interfaces*, 2019, **6**, 1802004.

18 Y. Luo, C. Yang, Y. Tian, Y. Tang, X. Yin and W. Que, *J. Power Sources*, 2020, **450**, 227694.

19 Z. Li, J. Dai, Y. Li, C. Sun, A. Meng, R. Cheng, J. Zhao, M. Hu and X. Wang, *Nano Res.*, 2022, **15**, 3213–3221.

20 A. Ali, J. Jo, Y. J. Yang and K. H. Choi, *Appl. Phys. A*, 2014, **114**, 323–330.

21 Y. Gogotsi and B. Anasori, *ACS Nano*, 2019, **13**, 8491–8494.

22 M. Das and S. Ghosh, *J. Phys. Chem. C*, 2024, **128**, 1014–1023.

23 M. Shariq, K. Alshehri, S. Mohammed Bouzgarrou, S. Kashif Ali, Y. Alqurashi, K. F. Hassan and R. E. Azooz, *FlatChem*, 2024, **44**, 100609.

24 A. Lipatov, M. Alhabeb, M. R. Lukatskaya, A. Boson, Y. Gogotsi and A. Sinitskii, *Adv. Electron. Mater.*, 2016, **2**, 1600255.

25 A. Miranda, J. Halim, M. W. Barsoum and A. Lorke, *Appl. Phys. Lett.*, 2016, **108**(3), 033102.

26 C. Qiao, H. Wu, X. Xu, Z. Guan and W. Ou-Yang, *Adv. Mater. Interfaces*, 2021, **8**, 2100903.

27 A. Ali, A. Belaidi, S. Ali, M. I. Helal and K. A. Mahmoud, *J. Mater. Sci.: Mater. Electron.*, 2016, **27**, 5440–5445.

28 Q. Wu, T. He, Y. Zhang, J. Zhang, Z. Wang, Y. Liu, L. Zhao, Y. Wu and F. Ran, *J. Mater. Chem. A*, 2021, **9**, 24094–24147.

29 S. Savitha, S. Surendhiran, K. S. Balu and A. Karthik, *Polym. Adv. Technol.*, 2024, **35**, e6215.

30 Y. Qiao, J. He, Y. Zhou, S. Wu, X. Li, G. Jiang, G. Jiang, M. Demir and P. Ma, *ACS Appl. Mater. Interfaces*, 2023, **15**(45), 52381–52391.

31 Z. Jiao, Y. Chen, M. Du, M. Demir, F. Yan, Y. Zhang, C. Wang, M. Gu, X. Zhang and J. Zou, *J. Alloys Compd.*, 2023, **958**, 170489.

32 G. Liu, L. Liu, G. Li, S. Wu, J. He, Y. Zhou, M. Demir and P. Ma, *Chem.–Eur. J.*, 2024, **30**, e202303267.

33 R. Xu, P. Ma, G. Liu, Y. Qiao, R. Hu, L. Liu, M. Demir and G. Jiang, *Energy Fuels*, 2023, **37**(8), 6158–6167.

34 Z. Li, C. Ma, Y. Wen, Z. Wei, X. Xing, J. Chu, C. Yu, K. Wang and Z.-K. Wang, *Nano Res.*, 2020, **13**, 196–202.

35 I. Rabani, J. Yoo, H.-S. Kim, D. V. Lam, S. Hussain, K. Karuppasamy and Y.-S. Seo, *Nanoscale*, 2021, **13**, 355–370.

36 G. M, S. G, M. A and A. V, *Appl. Surf. Sci.*, 2017, **403**, 578–583.

37 Y. Lu, B. Deng, Y. Liu, J. Wang, Z. Tu, J. Lu, X. Xiao and G. Xu, *Mater. Lett.*, 2021, **285**, 129101.

38 C. Yuan, L. Chen, B. Gao, L. Su and X. Zhang, *J. Mater. Chem.*, 2009, **19**, 246–252.

39 R. Tummala, R. K. Guduru and P. S. Mohanty, *J. Power Sources*, 2012, **209**, 44–51.

40 Z.-Y. Li, P. T. M. Bui, D.-H. Kwak, M. S. Akhtar and O. B. Yang, *Ceram. Int.*, 2016, **42**, 1879–1885.

41 S. Aslam, S. M. Ramay, A. Mahmood, G. M. Mustafa, S. Zawar and S. Atiq, *J. Sol-Gel Sci. Technol.*, 2023, **105**, 360–369.

42 S. Xu, X. Zhao, M. Zhang, X. Xu, X. Sun and Z. Luo, *Adv. Compos. Hybrid Mater.*, 2024, **7**, 1–15.

43 A. Karthikeyan and R. Mariappan, *J. Alloys Compd.*, 2023, **968**, 172094.

44 K. Athira, S. Dhanapandian, S. Suthakaran, S. Shobika, K. Yogalakshmi, M. Ayyar and M. Iqbal, *Z. Phys. Chem.*, 2024, **238**, 615–629.

45 S. Kalpana, V. S. Bhat, G. Hegde, T. N. Prabhu and P. N. Anantharamaiah, *Chem. Pap.*, 2024, **78**, 343–356.

46 R. Desai, V. Jadhav, P. Patil and D. Dalavi, *Mater. Adv.*, 2024, **5**, 920–960.

47 Y. Qu, M. M. Gomaa, M. H. Sayed, M. Boshta, G. Greczynski, R. Yakimova and J. Sun, *Adv. Mater. Interfaces*, 2024, **11**, 2300920.

48 M. Al-Gharram and T. AlZoubi, *Ceram. Int.*, 2024, **50**, 5473–5482.

49 S. Teke, M. M. Hossain, R. M. Bhattarai, S. Saud, A. Denra, M. C. Hoang Phuong Lan Nguyen, A. Ali, V. T. Nguyen and Y. S. Mok, *Nanoscale Adv.*, 2023, **5**, 3964–3975.

50 Z. Li, P. Wang, C. Ma, F. Igbari, Y. Kang, K.-L. Wang, W. Song, C. Dong, Y. Li, J. Yao, D. Meng, Z.-K. Wang and Y. Yang, *J. Am. Chem. Soc.*, 2021, **143**, 2593–2600.

51 P. W. Menezes, A. Indra, V. Gutkin and M. Driess, *Chem. Commun.*, 2017, **53**, 8018–8021.

52 C. Alex, S. C. Sarma, S. C. Peter and N. S. John, *ACS Appl. Energy Mater.*, 2020, **3**, 5439–5447.

53 S. Xie, Y. Liu, J. Deng, J. Yang, X. Zhao, Z. Han, K. Zhang and H. Dai, *J. Catal.*, 2017, **352**, 282–292.

54 J. Yang, H. Liu, W. N. Martens and R. L. Frost, *J. Phys. Chem. C*, 2010, **114**, 111–119.

55 R. Guo, R. Wang, Z. Ni and X. Liu, *Appl. Phys. A*, 2018, **124**, 623.

56 J. L. Gautier, E. Rios, M. Gracia, J. F. Marco and J. R. Gancedo, *Thin Solid Films*, 1997, **311**, 51–57.

57 L.-Å. Näslund, P. O. Å. Persson and J. Rosen, *J. Phys. Chem. C*, 2020, **124**, 27732–27742.

58 L.-Å. Näslund and I. Persson, *Appl. Surf. Sci.*, 2022, **593**, 153442.

59 I. Persson, L.-Å. Näslund, J. Halim, M. W. Barsoum, V. Darakchieva, J. Palisaitis, J. Rosen and P. O. Å. Persson, *2D Materials*, 2017, **5**, 015002.

60 S. Hüfner, *Photoelectron Spectroscopy: Principles and Applications*, Springer Science & Business Media, 2013.

61 L.-Å. Näslund, M.-H. Mikkelä, E. Kokkonen and M. Magnuson, *2D Materials*, 2021, **8**, 045026.

62 V. Natu, M. Benchakar, C. Canaff, A. Habrioux, S. Celerier and M. W. Barsoum, *Matter*, 2021, **4**, 1224–1251.

63 L. Mei, T. Yang, C. Xu, M. Zhang, L. Chen, Q. Li and T. Wang, *Nano Energy*, 2014, **3**, 36–45.

64 H. Shao, K. Xu, Y.-C. Wu, A. Iadecola, L. Liu, H. Ma, L. Qu, E. Raymundo-Piñero, J. Zhu, Z. Lin, P.-L. Taberna and P. Simon, *ACS Energy Lett.*, 2020, **5**, 2873–2880.

65 Z. Lin, E. Goikolea, A. Balducci, K. Naoi, P. L. Taberna, M. Salanne, G. Yushin and P. Simon, *Mater. Today*, 2018, **21**, 419–436.

66 Y. Wu and R. Holze, *Electrochem. Energy Technol.*, 2021, **7**, 1–37.

67 C. Kamaja, S. Mitra, G. Singh and M. Katiyar, *Energy Fuels*, 2021, **36**(1), 703–709.

68 J. V. Lima, H. G. Lemos, R. A. Silva, J. H. Rossato, M. H. Boratto and C. F. Graeff, *J. Alloys Compd. Commun.*, 2024, **3**, 100007.

69 X. Mu, D. Wang, F. Du, G. Chen, C. Wang, Y. Wei, Y. Gogotsi, Y. Gao and Y. Dall'Agnese, *Adv. Funct. Mater.*, 2019, **29**, 1902953.

70 M. Hu, Z. Li, T. Hu, S. Zhu, C. Zhang and X. Wang, *ACS Nano*, 2016, **10**, 11344–11350.

71 R. Ping, Y. Nie, C. Ji, Z. Hao, S. Yang, L. Li, J. Peng and X. Li, *Chem. Eng. J.*, 2023, **455**, 140650.

72 Y. Sun, J. Liansheng, D. Han, F. Wang, P. Zhang, H. Li and L. Niu, *Mater. Des.*, 2019, **188**, 108440.

73 T. C. Liu, W. G. Pell, B. E. Conway and S. L. Roberson, *J. Electrochem. Soc.*, 1998, **145**, 1882.

74 B. E. Conway and D. C. W. Kannangara, *J. Electrochem. Soc.*, 1987, **134**, 906.